Supplement

Figure S1. (a) Size resolved relative errors (systematic errors/uncorrected net flux) for signal attenuation in the sampling line, limited response time, particle losses in the sampling line, the Webb correction, Kowalski correction and modelled aerosol dry deposition flux. (b) Size-resolved uncorrected median net flux, fully corrected median net flux and median emission flux. The insets show the ratio of the fully corrected to uncorrected net flux and the ratio of emission flux to fully corrected net flux.
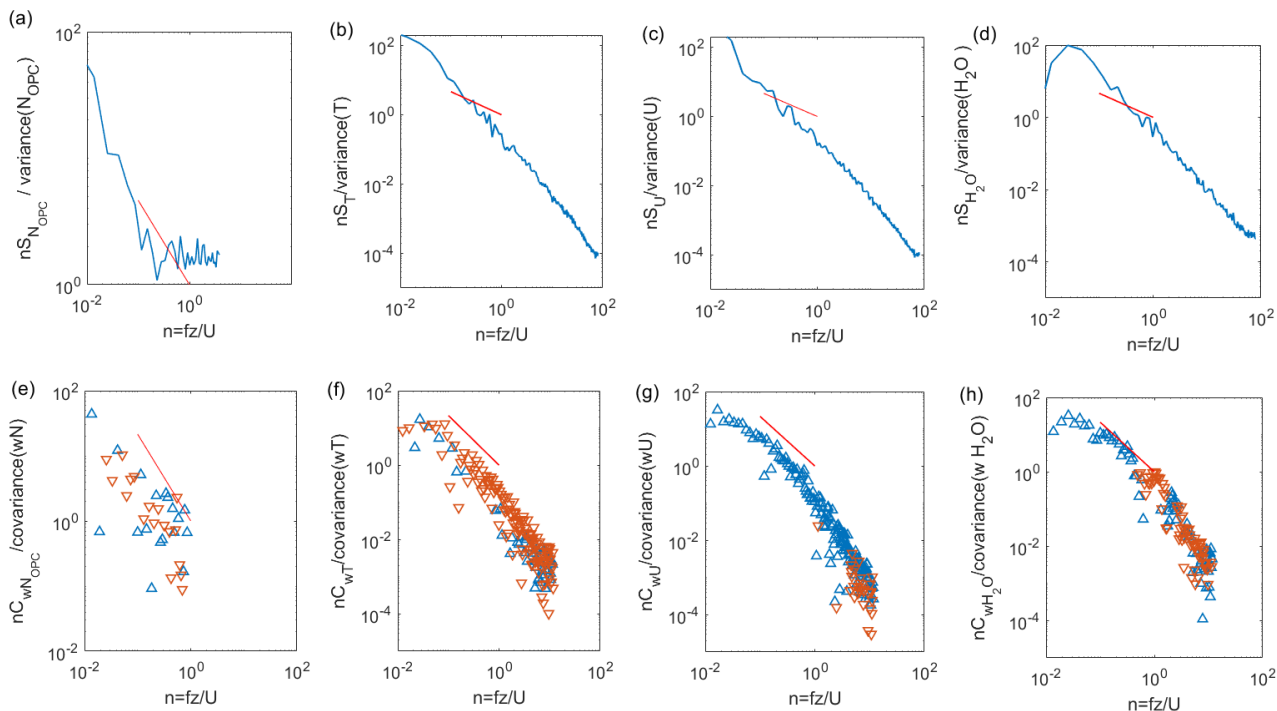
Figure S2. Normalised power spectra for (a) particle concentration measured with the OPC, (b) temperature, (c) horizontal wind, and (d) water vapor (H_2O) plotted against the dimensionless frequency. The red lines indicate the -2/3 slope, which represents the theoretical decay within the inertial subrange. Normalised co-spectra of vertical wind (e) particle concentration measured with the OPC, (f) temperature, (g) horizontal wind, and (h) water vapor (H_2O) plotted against the dimensionless frequency. The red lines indicate the -4/3 slope that is representative of the theoretical decay within the inertial subrange.

References

Norris, S. J., Brooks, I. M., de Leeuw, G., Smith, M. H., Moerman, M. M., and Lingard, J. J.: Eddy covariance measurements of sea spray particles over the Atlantic Ocean, Atmos. Chem. Phys., 8, 555–563, https://doi.org/10.5194/acp-8-555-2008, 2008.

Rosati, B., Wehrle, G., Gysel, M., Zieger, P., Baltensperger, U., and Weingartner, E.: The white-light humidified optical particle spectrometer (WHOPS) – a novel airborne system to characterize aerosol hygroscopicity, Atmos. Meas. Tech., 8, 921–939, https://doi.org/10.5194/amt-8-921-2015, 2015.
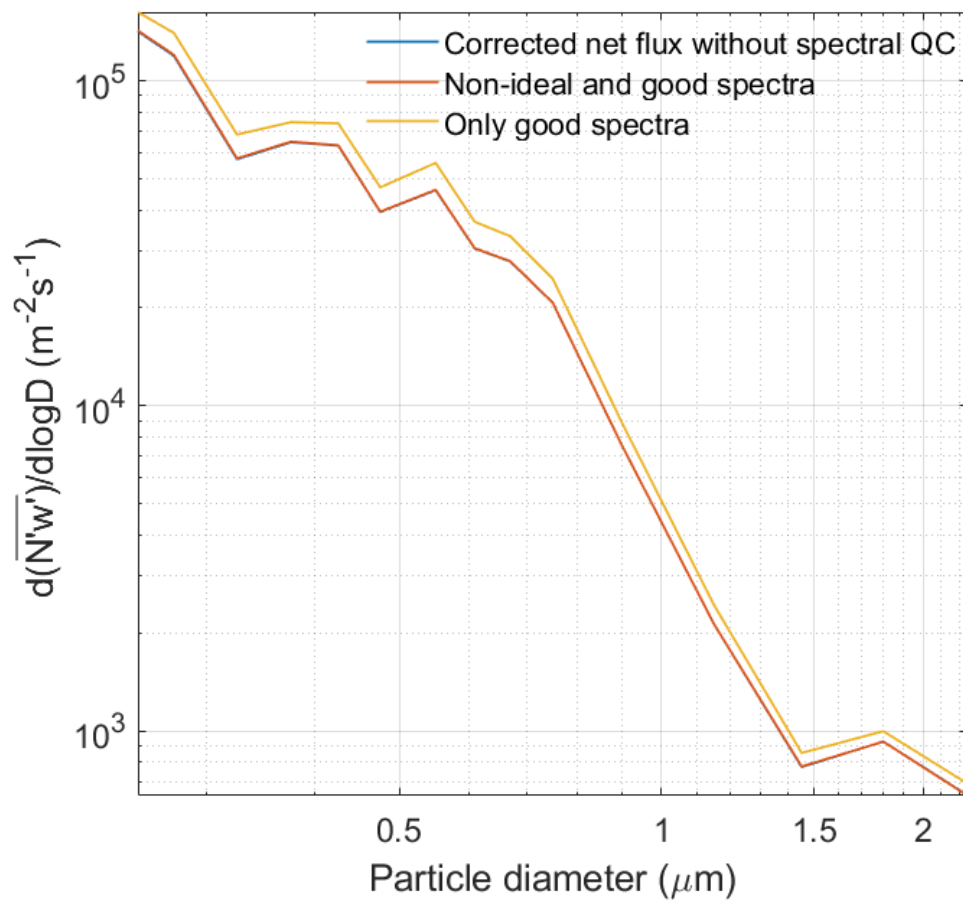
Figure S3. Effect of spectral analysis on the emission flux size distribution measured on Östergarnsholm.
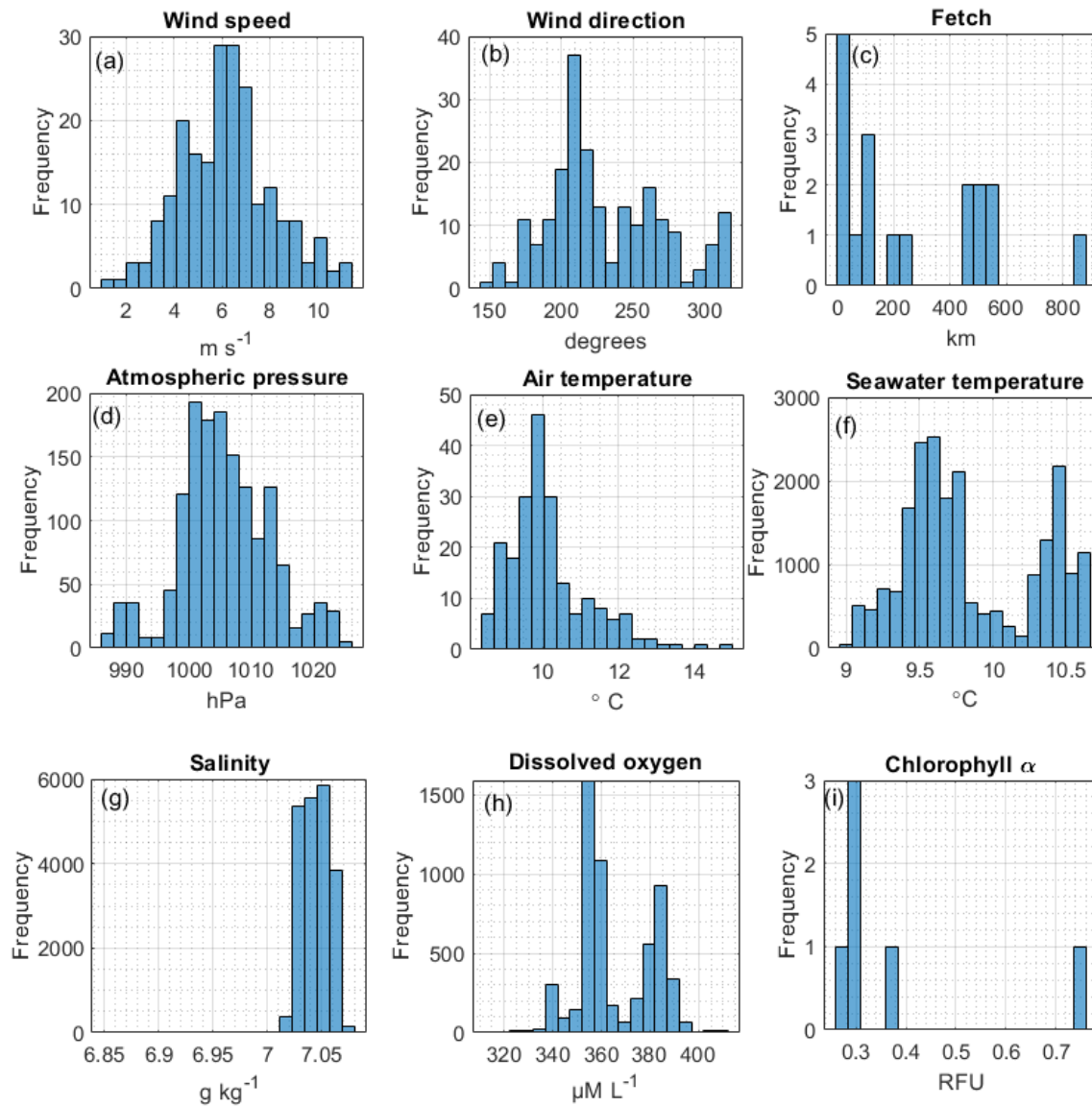
Figure S4. Overview of the synoptical situation during the Oceania campaign, (a) wind speed, (b) wind direction, (c) fetch, (d) atmospheric pressure, (e) air temperature, (f) seawater temperature, (g) seawater salinity, (h) dissolved oxygen concentration in the seawater and (i) concentration of chlorophyll-α in reference fluorescence units (RFU) in the seawater.
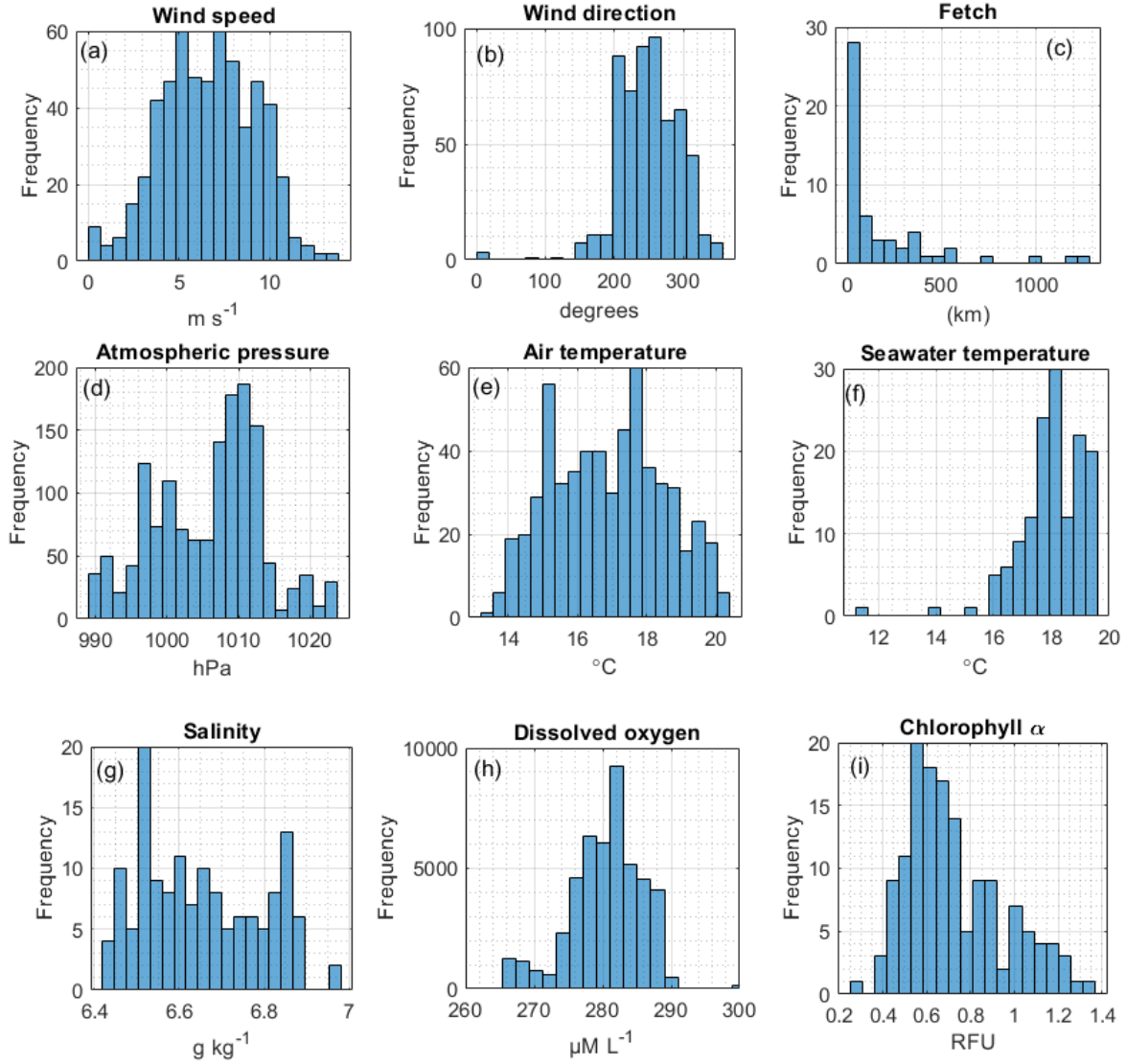
Figure S5. Overview of the synoptical situation during the Electra campaign, (a) wind speed, (b) wind direction, (c) fetch, (d) atmospheric pressure, (e) air temperature, (f) seawater temperature, (g) seawater salinity, (h) dissolved oxygen concentration in the seawater and (i) concentration of chlorophyll-α in reference fluorescence units (RFU) in the seawater.
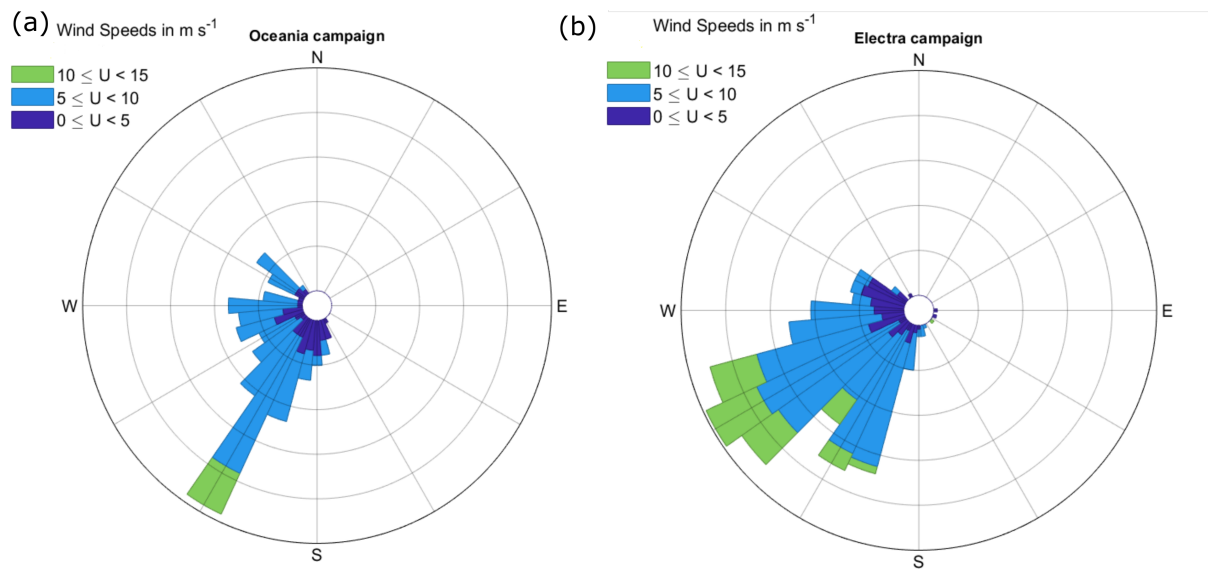
Figure S6. Prevailing wind speeds and directions during the Oceania campaign in May (a) and Electra campaign in August (b).
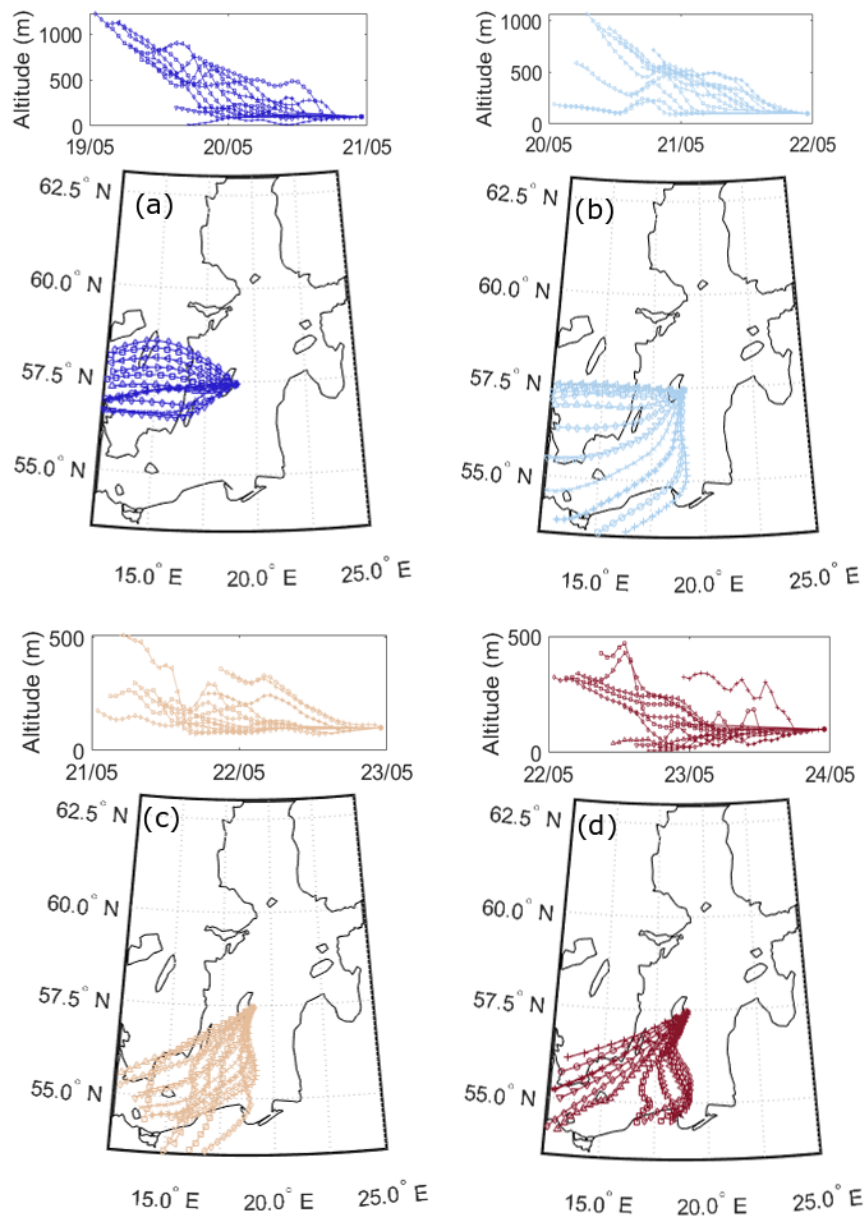
Figure S7. Hysplit 24-hour backward trajectories (every second hour) for sampling days when Oceania was located close to the station.
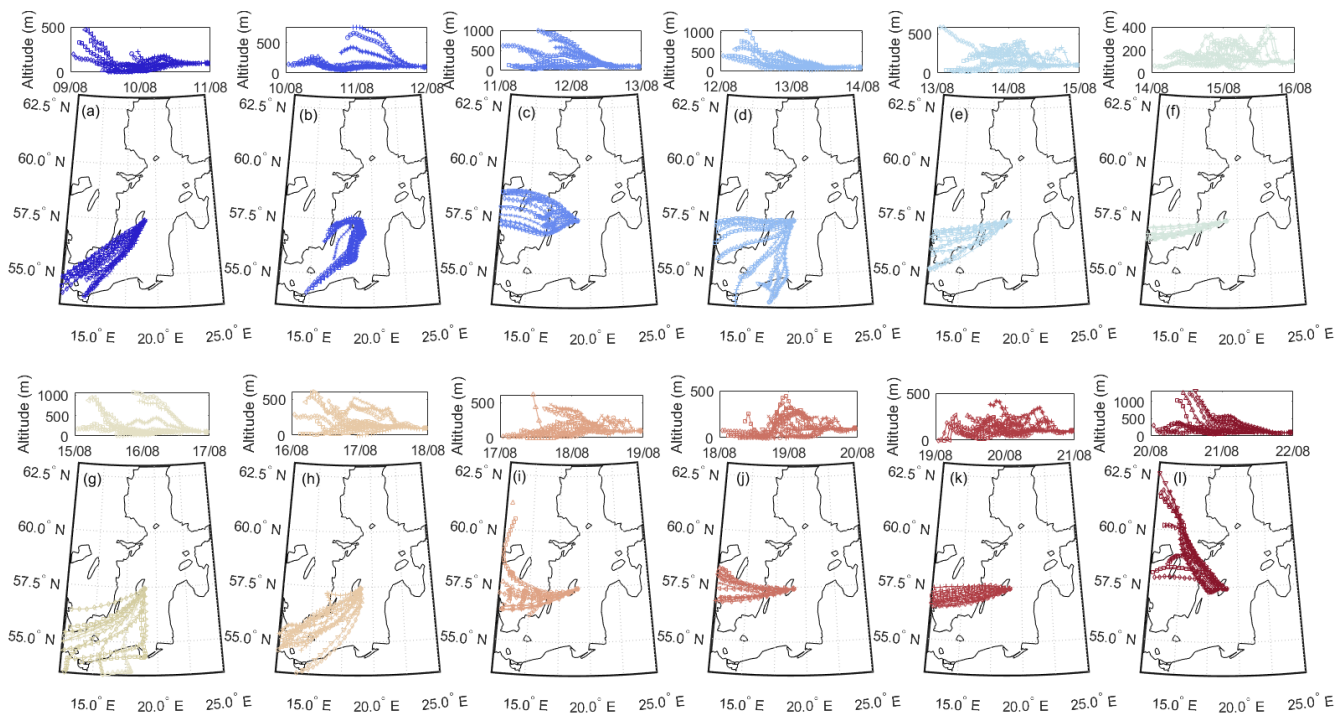
Figure S8. Hysplit 24-hour backward trajectories (every second hour) for sampling days when Electra was located close to the station.
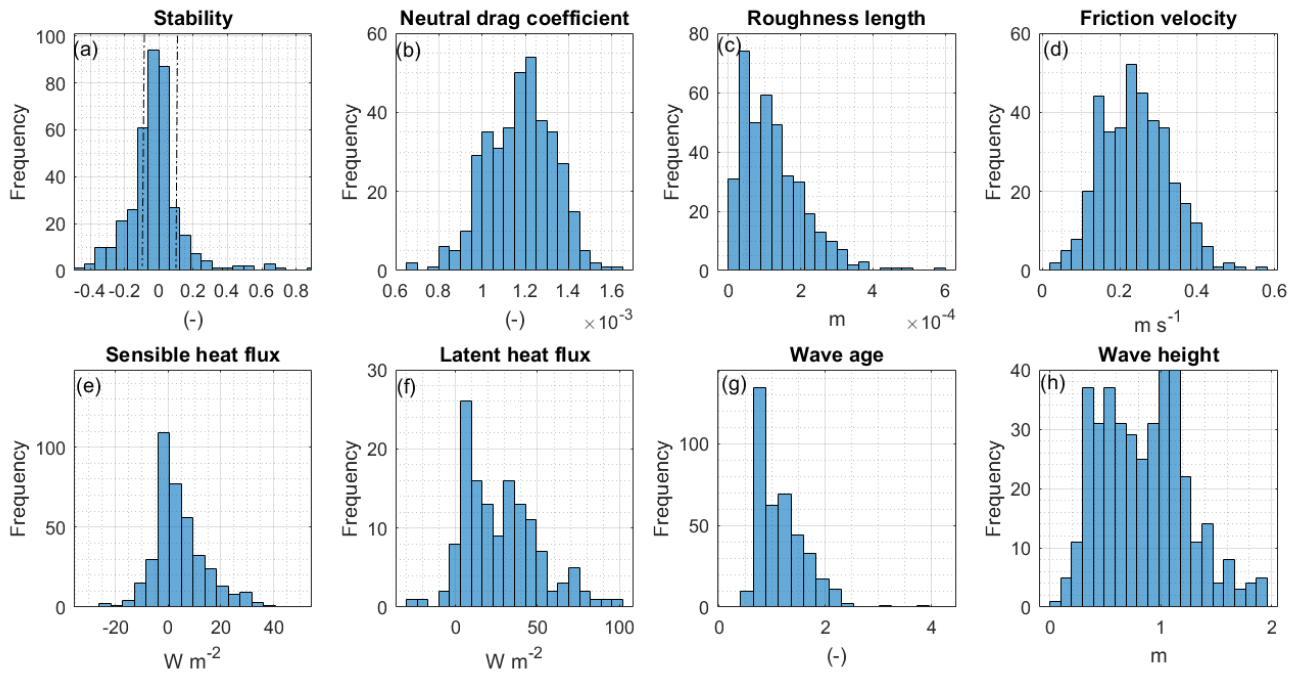
Figure S9. Histograms of micrometeorological parameters for campaigns combined. (a) Stability, (b) neutral drag coefficient, (c) roughness length, (d) friction velocity, (e) sensible heat flux, (f) latent heat flux, (g) wave age and (h) wave height. Only data from the open sea sector is shown. The dashed line in panel (a) indicates stable ($\frac{z}{L} > 0.1$), neutral ($-0.1 < \frac{z}{L} < 0.1$) and unstable ($-0.1 < \frac{z}{L}$) conditions.
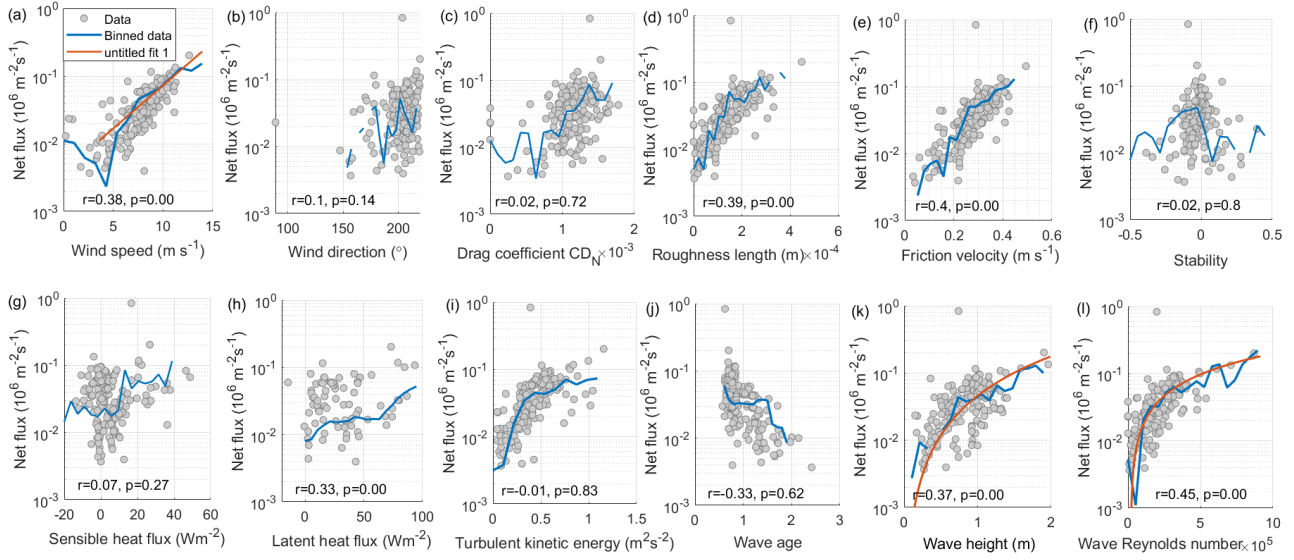
Figure S10. Scatterplots of the net aerosol flux $\overline{N'w'}$ from the open sea sector with (a) wind speed $U_{10\,\mathrm{m}}$, (b) wind direction, (c) drag coefficient CD_N, (d) roughness length z_0, (e) friction velocity $u*$, (f) stability $\frac{z}{L}$, (g) sensible heat flux H, (h) latent heat flux λE, (i) turbulent kinetic energy TKE, (j) wave age, (k) wave height and (l) wave Reynolds number. The grey dots show all data points, blue lines show binned data and orange lines show a log-linear fit $\log(\overline{N'w'}) = 0.13 \cdot U - 2.4$, $r^2 = 0.5$ between net flux and wind speed, a power-law fit $\overline{N'w'} = 0.05 \cdot H_s^{1.93}$, $r^2 = 0.42$ between the net flux and wave height and a linear fit $\overline{N'w'} = 2.1 \cdot 10^{-7} \cdot ReH_w - 3.3 \cdot 10^{-3}$, $r^2 = 0.52$ between the net flux and the wave Reynolds number. The correlation coefficients r and levels of significance p for each parameter with the EC flux are given in each panel.
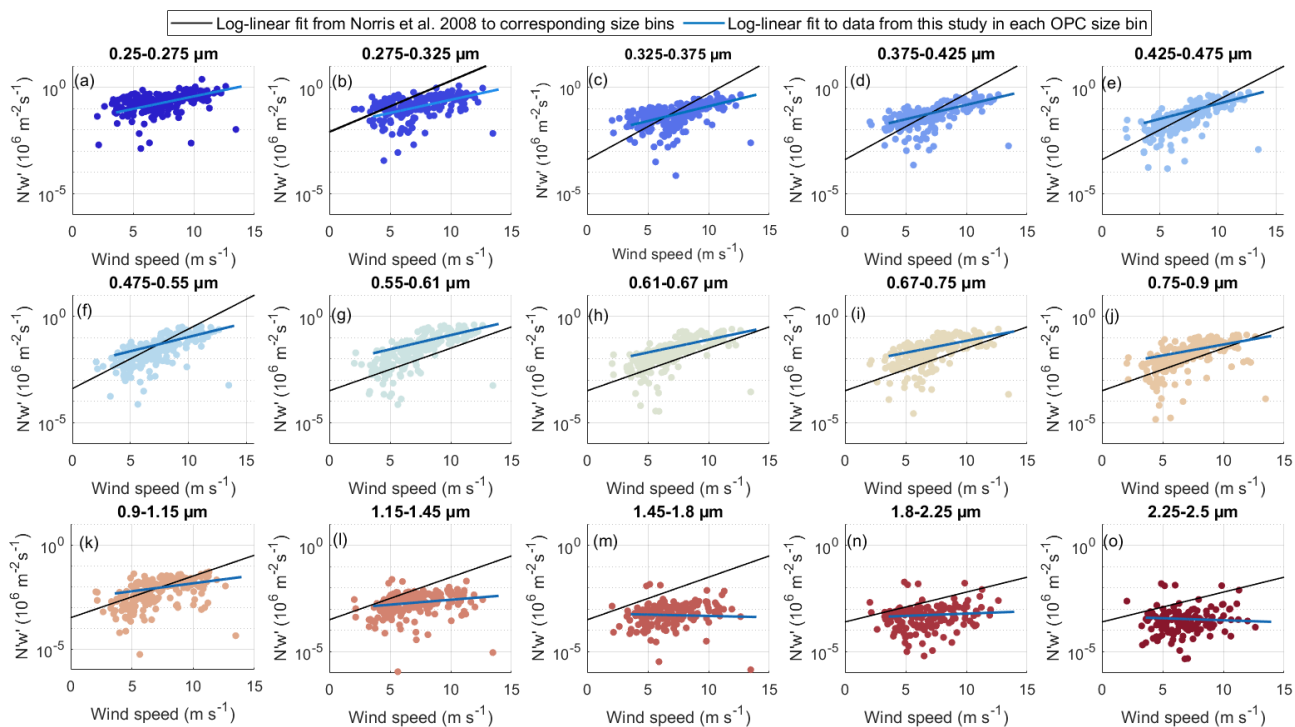
Figure S11. (a)-(o) Dependence of the in situ EC fluxes in different size bins on wind speed with log-linear fits (the coefficients for each fit are provided in Fig. 12. The fits for aerosol EC fluxes from Norris et al. (2008) are added for matching size bins.
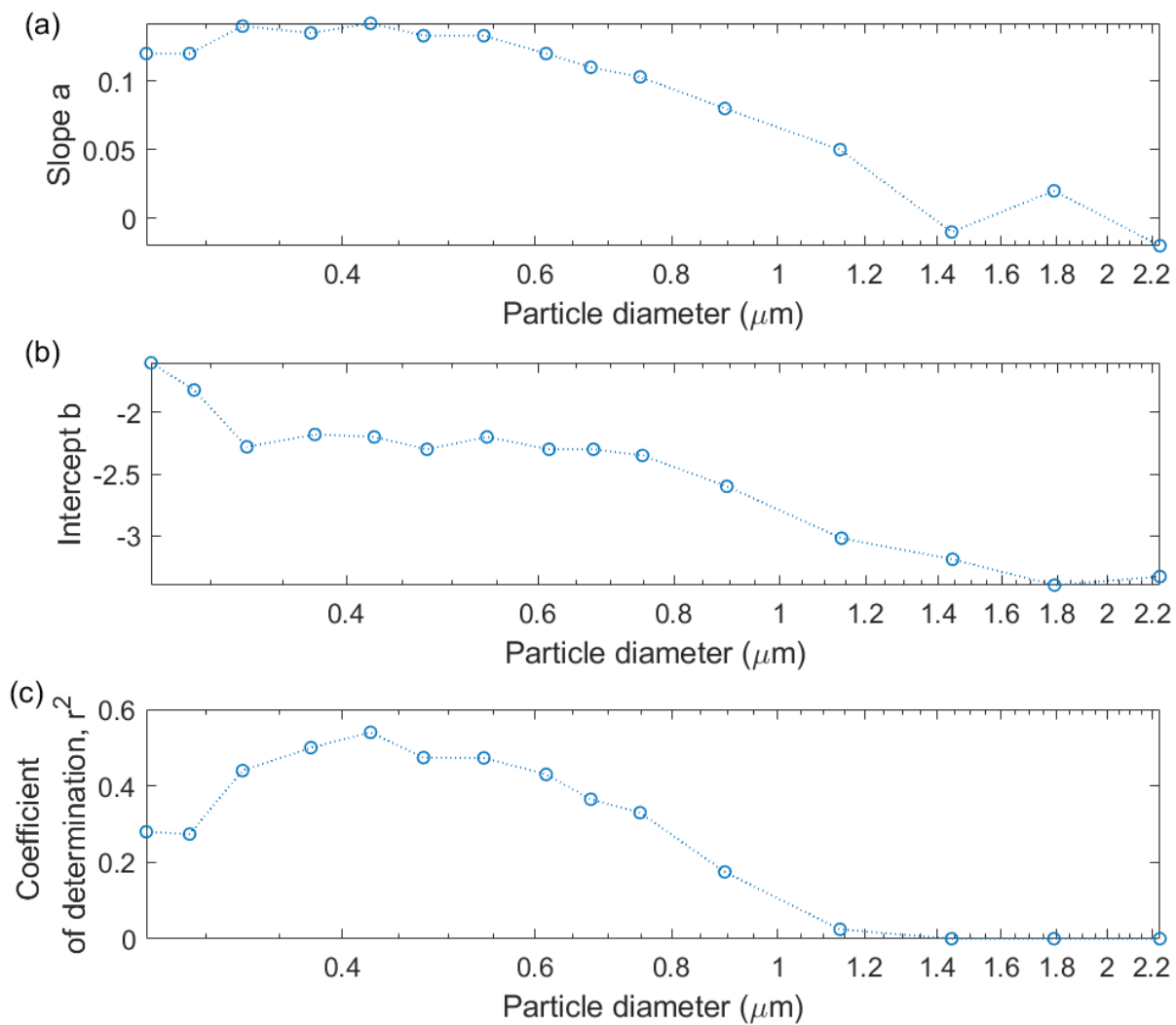
Figure S12. (a) Slope a, (b) intercept b and (c) coefficient of determination r^2 for the size-resolved log-linear fits with wind speed (equation **??**) for both emission and EC fluxes.
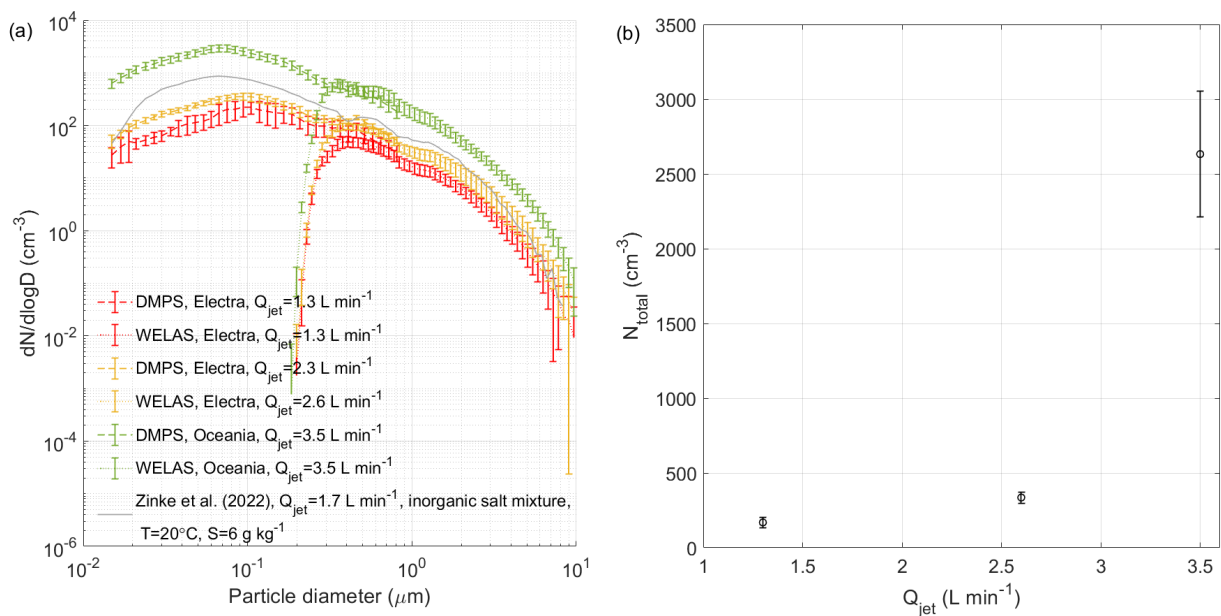
Figure S13. (a) Overlap between the number size distributions measured by the DMPS and WELAS for different jet flow rates and (b) total concentrations of particles measured in the headspace of the sea spray simulation chamber at different jet speeds. Values are given as mean and standard deviation. The WELAS reaches $100\,\%$ counting efficiency for particles with diameters larger than 0.3 μm (Rosati et al., 2015), which is why the size distributions measured by the DMPS and WELAS were combined at 0.35 μm.
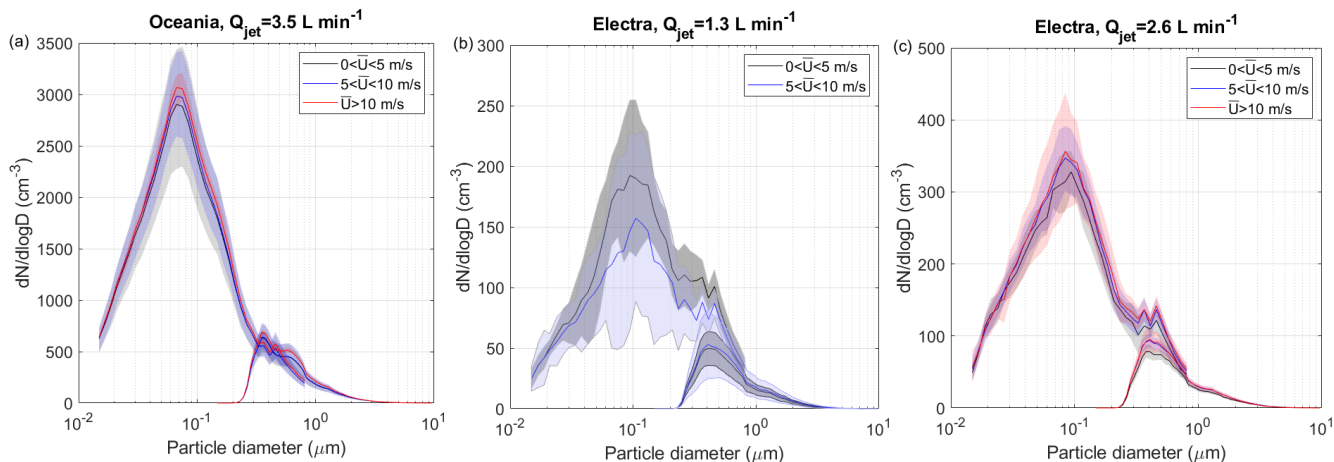
Figure S14. Effect of wind speed on the particle concentration in the head space of the sea spray simulation chamber a) at a jet flow of 3.5 L min^{-1} speed during the Oceania campaign, b) at a jet flow of 1.3 L min^{-1} during the Electra campaign and c) at a jet flow of 2.6 L min^{-1} during the Electra campaign. Values are depicted as mean and standard deviation. mean and standard deviation. At particle diameters below 0.3 μm, the counting efficiency is less than 100 % (Rosati et al., 2015), which is why the WELAS was only used for particles diameters > 0.35 μm.
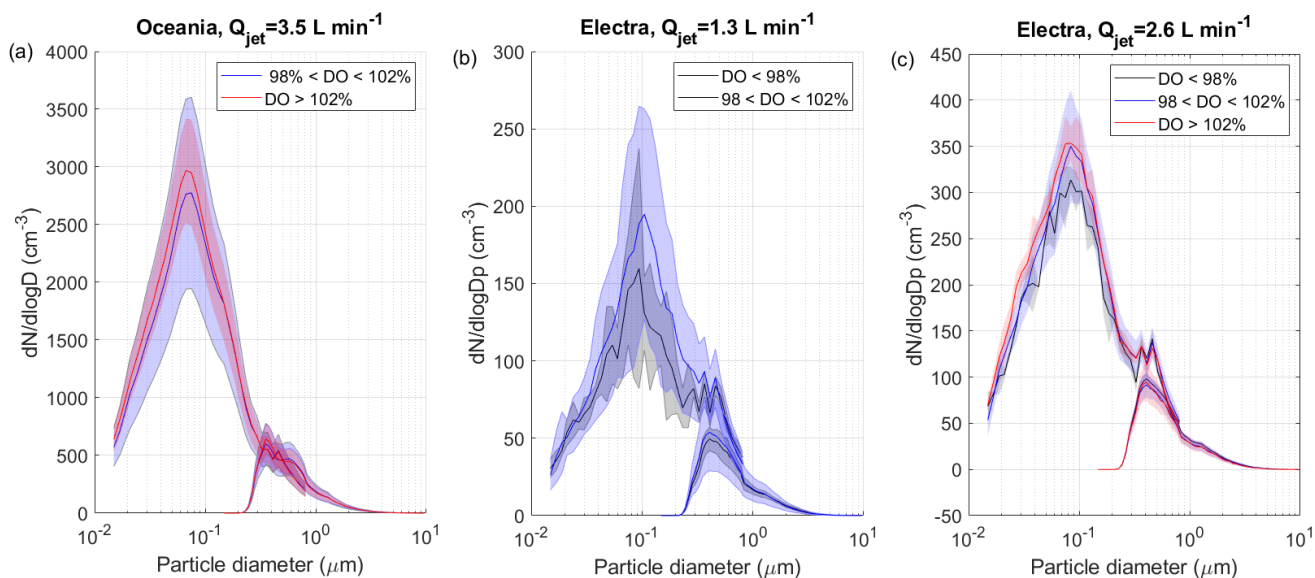
Figure S15. Effect of dissolved oxygen (DO) saturation on the particle concentration in the head space of the sea spray simulation chamber a) at a jet flow of 3.5 L min^{-1} during the Oceania campaign, b) at a jet flow of 1.3 L min^{-1} during the Electra campaign and c) at a jet flow of 2.6 L min^{-1} during the Electra campaign. Values are depicted as mean and standard deviation.
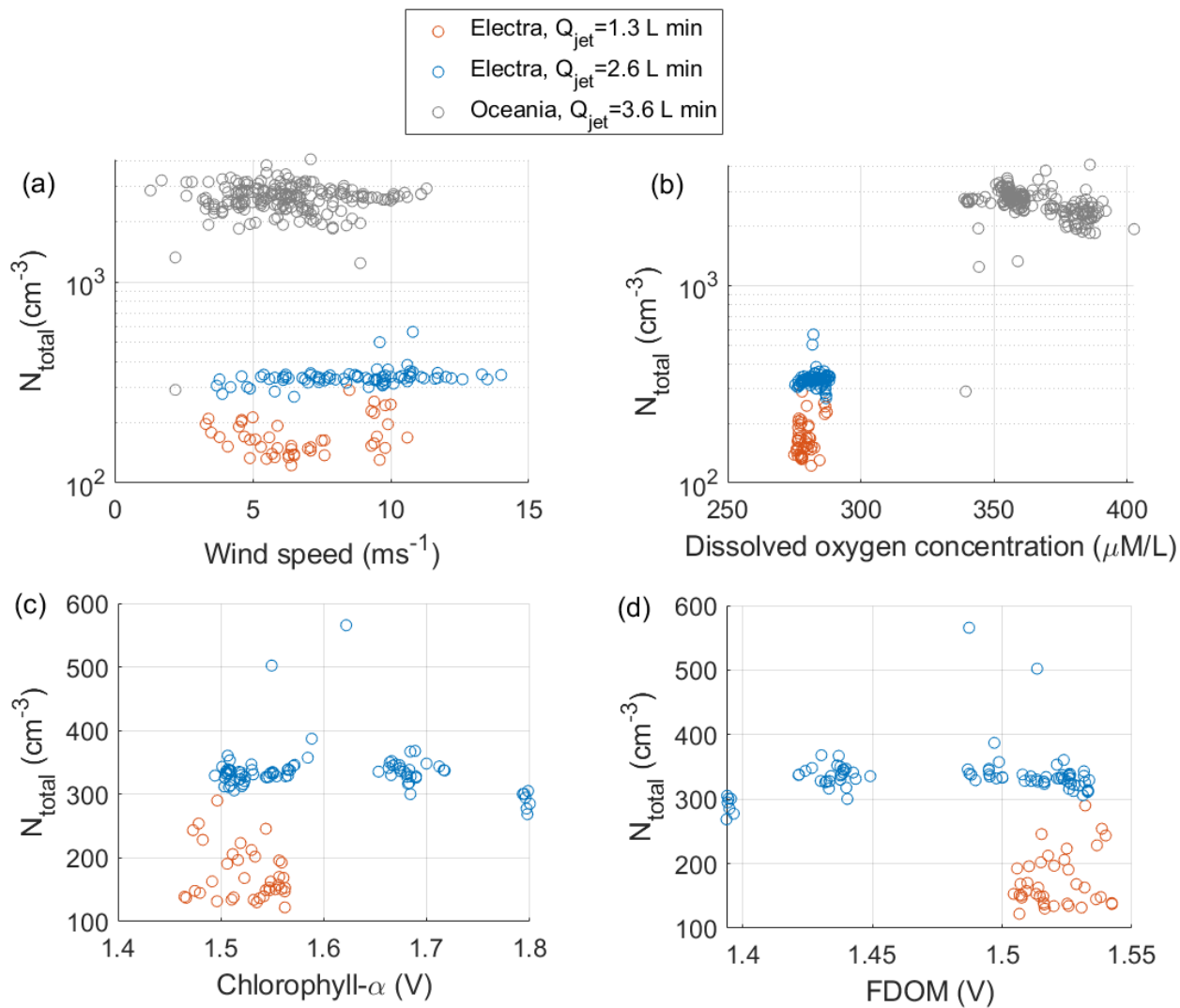
Figure S16. Dependence of particle concentration in the headspace of the sea spray simulation chamber during on (a) wind speed, (b) dissolved oxygen concentration, (c) chlorophyll-α and (d) FDOM. The chlorophyll-α and FDOM concentrations are given in volt (V) measured by the fluorometer.
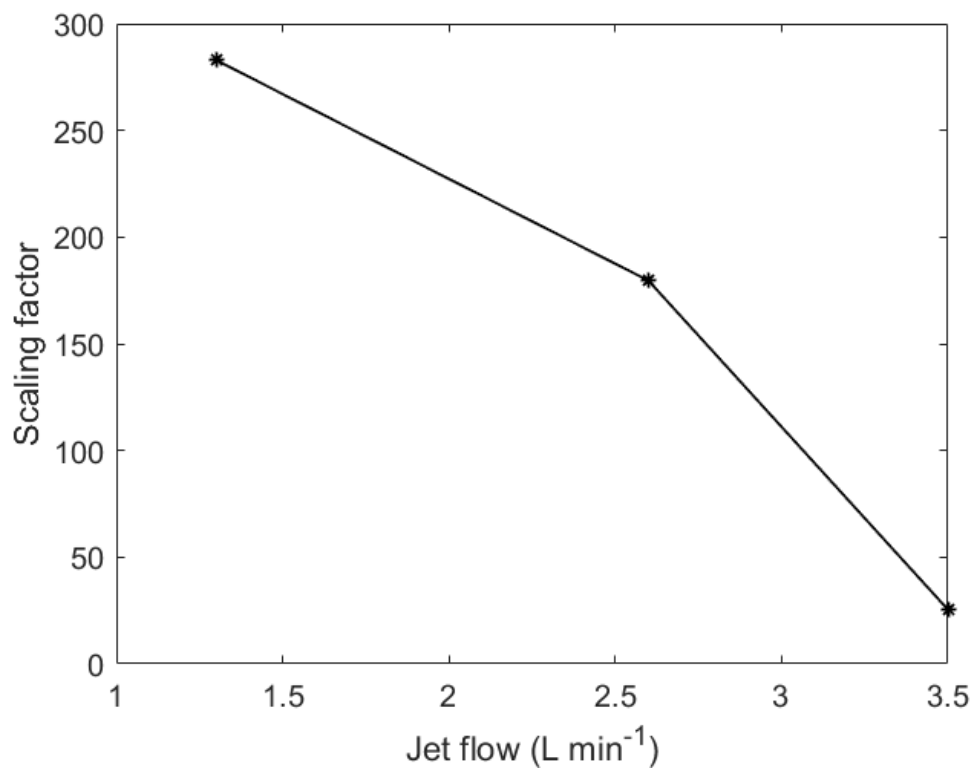
Figure S17. Dependence of the scaling factor on jet flow rate.
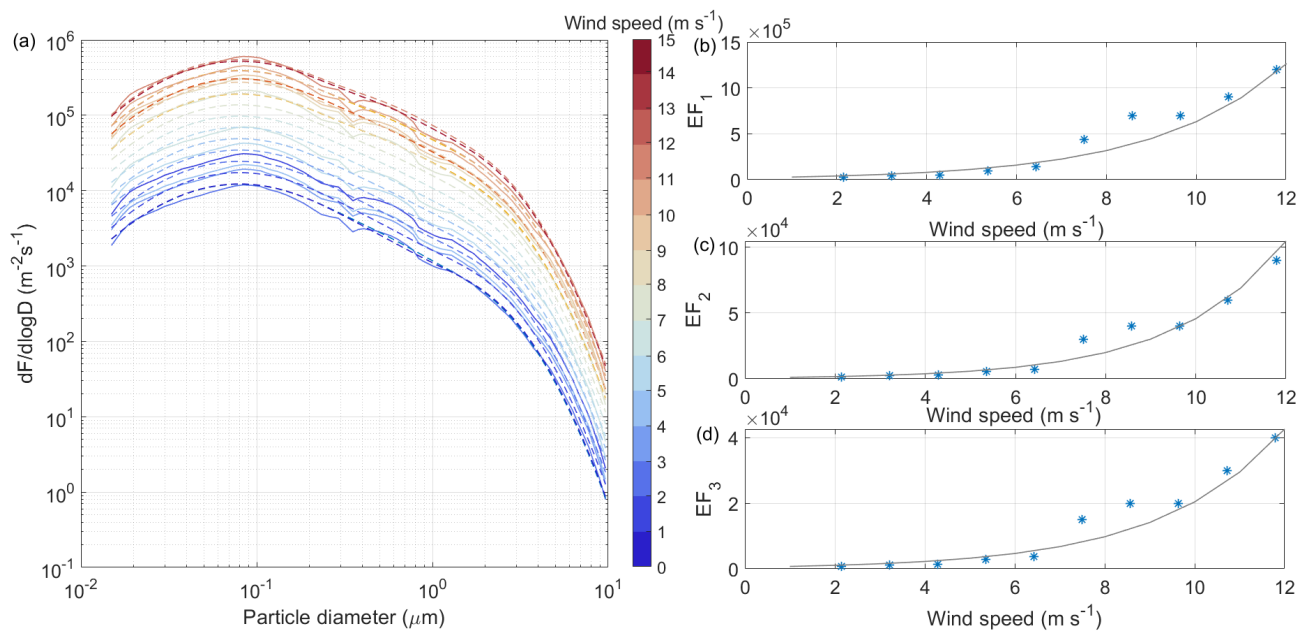
Figure S18. (a) Measured (solid lines) and parameterised (dashed lines) emission flux in dependence on wind speed, (b)-(d) log-linear fits to the emission magnitude in each mode with increasing wind speed.
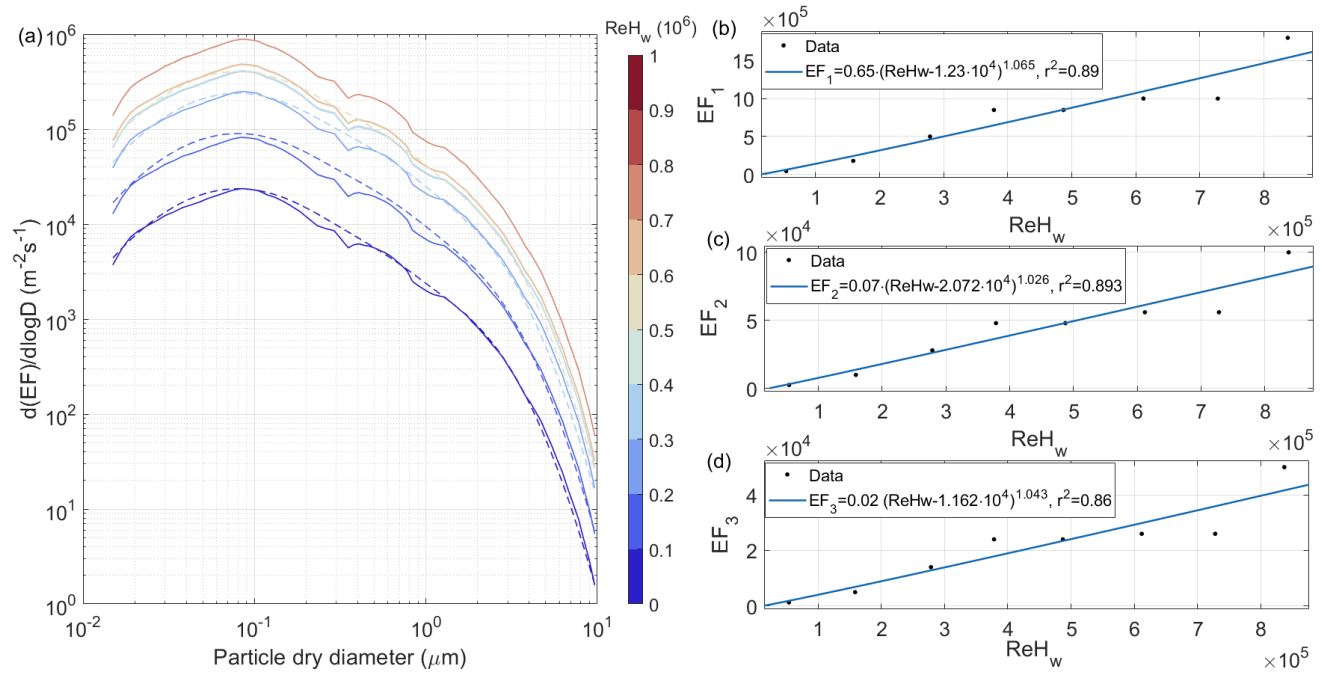
Figure S19. (a) Measured (solid lines) and parameterised (dashed lines) emission flux in dependence on wave Reynolds number, (b)-(d) Fits to the emission magnitude in each mode with increasing wave Reynolds number.
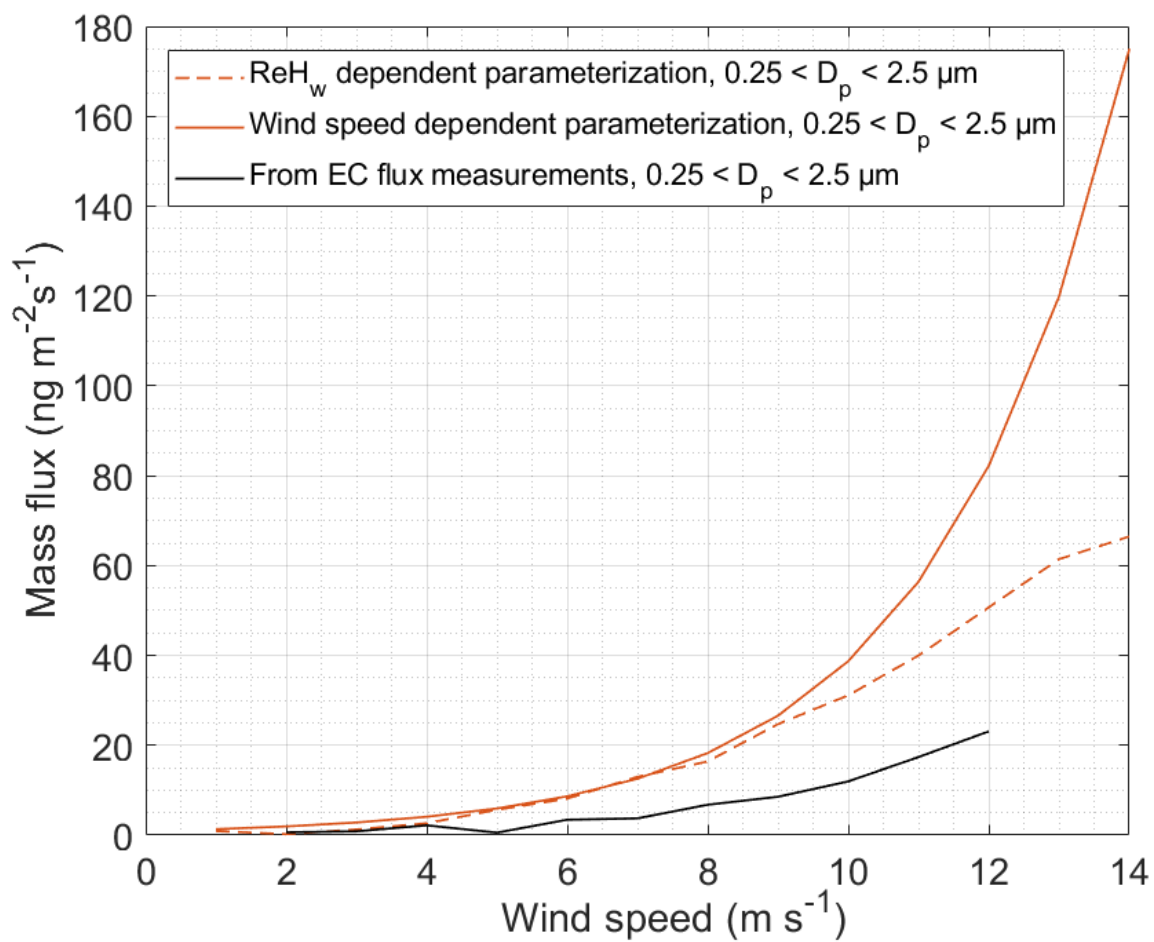
Figure S20. Comparison of mass flux estimates from the wave Reynolds number dependent and wind speed dependent parameterizations with mass flux estimates from the in-situ measurements.